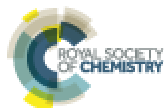

Journal of Materials Chemistry A

Creating stable interfaces between reactive materials: Titanium nitride protects photoabsorber-catalyst interface in water-splitting photocathodes

Journal:	*Journal of Materials Chemistry A*
Manuscript ID	TA-ART-12-2018-012186.R1
Article Type:	Paper
Date Submitted by the Author:	03-Jan-2019

Complete List of Authors:	Hwang, Shinjae; Rutgers The State University of New Jersey, Chemistry & Chemical Biology Porter, Spencer; Rutgers The State University of New Jersey, Department of Chemistry & Chemical Biology Laursen, Anders; Rutgers, the State University of New Jersey, Chemistry and Chemical Biology Yang, Hongbin; Rutgers The State University of New Jersey, Chemistry and Chemical Biology Li, Mengjun; Rutgers The State University of New Jersey, Chemistry & Chemical Biology Manichev, Viacheslav; Rutgers The State University of New Jersey, Chemistry & Chemical Biology Calvinho, Karin; Rutgers, The State University of New Jersey, Chemistry and Chemical Biology Amarasinghe, Voshadhi; Rutgers The State University of New Jersey, Chemistry & Chemical Biology Greenblatt, Martha; Rutgers The State University of New Jersey, Chemistry & Chemical Biology Garfunkel, Eric; Rutgers The State University of New Jersey, Chemistry and Chemical Biology Dismukes, Gerard; Rutgers University, Chemistry & Chemical Biology

SCHOLARONE™
Manuscripts

Creating stable interfaces between reactive materials: Titanium nitride protects photoabsorber-catalyst interface in water-splitting photocathodes

Shinjae Hwang[1], Spencer H. Porter[1], Anders B. Laursen[1], Hongbin Yang[1], Mengjun Li[1], Viacheslav Manichev[1], Karin U. D. Calvinho[1], Voshadhi Amarasinghe[1], Martha Greenblatt[1], Eric Garfunkel[1*], and G. Charles Dismukes[1,2*]

[1] Department of Chemistry & Chemical Biology, Rutgers, The State University of New Jersey, 610 Taylor Rd. Piscataway, NJ 08854, [2] The Waksman Institute, Rutgers, The State University of New Jersey, 190 Frelinghuysen Rd, Piscataway, NJ 08854.

*Corresponding authors: egarf@chem.rutgers.edu and dismukes@chem.rutgers.edu

ABSTRACT

The development of a solar-driven water splitting device that replaces costly precious metals, while achieving stable high performance, is a major challenge. Transition metal phosphides are active and low-cost catalysts for the hydrogen evolution reaction (HER), although, none thus far have exhibited stable performance when interfaced with semiconductors. Here, we report on a monolithic junction consisting of cubic-NiP_2:TiN:Si, fabricated using both commercial and custom Si photovoltaics. Stable performance is achieved using an ultrathin film of crystalline TiN that effectively hinders atomic diffusion between interfaces during fabrication. Crystalline cubic-NiP_2 deposited on TiN/n^+p-Si retains 97% of the bare Si photovoltage, comparable saturation current density as bare Si, and has a turnover frequency of 1.04 H_2 site^{-1}s^{-1} at −100 mV applied potential. In acid, it requires only −150 mV additional overpotential compared to the benchmark, Pt/TiN/n^+p-Si, to reach a HER

photocurrent density of −10 mA/cm^2. This photocathode maintains a stable H_2 photocurrent (±10%) for at least 125 hours, the duration of testing. When the same layers are fabricated on a commercial Si solar cell, this photocathode produced double the photocurrent density (36.3 mA/cm^2, under simulated 1.5 AM G illumination). Physical characterization gives detailed information on the properties responsible for the observed activity and durability of these interfaces. In general, the thin-film methodology presented here is widely applicable, demonstrates superior activity, and achieves long-term stability.

Keywords: Titanium nitride, nickel phosphide, ultra-thin film, hydrogen evolution, passivation layer, photoelectrochemical water splitting

Introduction

Hydrogen is a renewable energy carrier, and could potentially replace a fossil-fuel-based economy by using advanced fuel cell technology to recover the stored energy. [1] However, the predominant method to produce hydrogen today involves steam reforming of natural gas resulting in CO_2 production. [2] This has motivated significant research into the production of clean H_2 from water, without the release of CO_2. [3,4] Solar-driven water splitting is a potentially clean and renewable hydrogen production technology, because it absorbs sunlight and produces only hydrogen and oxygen as products. [5] Efficient water splitting devices use two or more photoabsorbers to obtain sufficient photovoltage for bias-free photoelectrochemical cell (PEC) operation. A tandem configuration PEC has two absorbers in series, one with a narrow bandgap and a second one with a wide bandgap, where the bandgaps are carefully matched to optimize absorption across the solar spectrum. [6-9] This configuration mimics the two photosystems found universally in natural oxygenic photosynthesis. Multijunction series-connected PV cells have also been demonstrated to achieve high solar-to-hydrogen efficiency as a photovoltaic-electrolysis (PV-EC) device configuration [10-14]

However, because most semiconductors that operate in the visible-NIR spectrum, such as Si, $GaInP_2$, and GaAs are unstable in water, a protective interfacial layer is required between the photoabsorber and the catalyst/electrolyte to maintain operation. Interfacial protection layers comprised of wide bandgap oxides (e.g., TiO_2, Al_2O_3) or 2D chalcogenides (e.g., MoS_2) have been demonstrated to be superior to direct contact for stability. [15-18] An alternative approach, a back illumination (illuminating the non-catalyst part) of PV-EC setup has also been attempted to help enable prolonged durability. [13,19,20] In addition, progress has been made towards replacing the archetypical (yet expensive and scarce) platinum catalyst, used for the hydrogen evolution reaction (HER), with non-noble catalysts. [21-23] However, successful integration of these reported catalysts to the underlying photoabsorbing semiconductors, while not compromising either materials performance and achieving long term passivation remains a very active research area for technology.

Silicon is a well-established photovoltaic material possessing excellent electronic properties including an optimal narrow bandgap which theory predicts is matched well to the narrow bandgap materials required for a tandem PEC. [7,24] Earlier studies investigated TiO_2 as a protection layer on a Si photoabsorber and under an amorphous MoS_x (or crystalline MoS_2) as catalyst, but insufficient exposure of MoS_2 HER-active edge sites hindered activity. [25,26] To increase the HER activity, vertically standing 2D-nanosheets of MoS_2 have been deposited on Si protected with an Al_2O_3 layer. Although relatively high saturated photocurrent density (~ 35.6 mA/cm^2) and relatively low onset voltage were achieved (V_{onset} 0.4 V vs. RHE), the low intrinsic HER activity of this MoS_2 polymorph requires high mass loading of catalysts to match up with the underlying high performance Si photoabsorber. [17]

Transition metal phosphide (TMP) catalysts show higher intrinsic HER activity than most non-noble HER catalysts, and a few of them such as Ni_5P_4, and $Fe_{0.5}Co_{0.5}P$ are currently recognized as state-of-the-art HER catalysts. [22,27-30] Nevertheless, few studies have demonstrated active TMP catalysts coupled with silicon light absorbers, mainly due to an

unstable catalyst/Si interface. [27,28] Hellstern, *et al.* [31] produced a CoP thin-film on a Si photoabsorber that outperforms MoS_2 on Si photoabsorber for HER. However, the authors noted the formation of silicon oxide during operation (after 24 hours), indicating the onset of photoabsorber degradation. Commercial applications in viable PEC devices require thousands of hours of durability. [31,3228,29] In a different approach, a thin film of cubic-NiP_2 was synthesized on a Ti adhesion layer on top of a silicon photoabosorber. [33] However, this method achieved similar photo/electrocatalytic activity compared to MoS_2 with similar catalyst loading and showed only 6 h of stability. [6,33] Ti does indeed provide good adhesion for the Ni layer, [34] but it is not a suitable diffusion barrier for Si, as seen by intermixing of Ti and Si even at the lowest temperature for catalyst synthesis (300 °C). [35]

To achieve a stable and active TMP catalyst/Si system, an understanding of metal silicide ($NiSi_x$, $CoSi_x$) chemistry is necessary. Metal silicides are conductive materials that have been explored previously for metal contacts in microelectronic devices. [36,37] Although nickel silicides are known as good metallic contacts (resistivity ~15 μΩ·cm), [38] they have two major drawbacks for PEC applications: First, if they become overly thick (> 30 nm) they will decrease transmissivity (T < 50 %), thus reducing the incident photon to H_2 efficiency. [39] Second, they form a native oxide upon air-exposure causing significantly increased junction impedance. [40] Furthermore, silicon diffusion interferes with the conversion of Ni to the nickel phosphide by consumption of the Ni source. Figure S1 (see electronic supplementary information) shows that the relatively low formation temperature of nickel silicide causes it to form at the interface between nickel and silicon. [36,41] Additionally, it was found that an oxide forms on the nickel silicide outer surface layer upon exposure to air. It is therefore clear that introducing a diffusion barrier between the active TMP catalyst and the Si absorber is indispensable to obtain stable interfaces between these desired materials.

Titanium nitride has been well investigated in microelectronic devices due to its unique combination of physical properties, such as high conductivity, corrosion resistance,

and extreme hardness. [42] It also has been used effectively as a diffusion barrier on silicon at high temperature because of an extremely low diffusivity of silicon (~10^{-20} m^2/s) — which is an order of magnitude lower than that of TiO_2 at the TMP formation temperature (400 – 600 °C) due to densely packed structure. [43] In the fuel cell research literature, some attempts have also been made to replace the carbon support with TiN due to its high corrosion resistance. [44,45] By contrast, only a few reports have gone on to utilize TiN as a catalyst in the PEC community. [4643] Moreover, none of them have used TiN as a protection layer. The high density of TiN and its low formation energy, [47,48] predicts it as an excellent passivation layer for the Si photoabsorber during HER. Furthermore, the work function of thin-film TiN (4.6 eV) also makes the conduction band minimum of TiN well aligned to degenerately-doped Si, thereby minimizing the junction impedance.

Herein, we report fabrication of a monolithic HER/photocathode junction comprised of cubic-NiP_2 thin-film, supported on a TiN/Si photocathode, with high turnover frequency (TOF), and exceptional stability in acidic media. Diffraction analysis establishes that the c-axis of cubic-NiP_2, deposited as a thin-film, is oriented normal to the interface which, in turn, may contribute to its high TOF. Comparing it to TiO_2, the TiN interfacial layer is demonstrated to be superior for prevention of Si diffusion during high temperature fabrication, creating a low impedance contact possessing high optical transparency, and providing long-term stability. Using this approach to fabricate a photoelectrochemical cell using commercial crystalline Si as photocathode, the resulting cubic-NiP_2/TiN/Si device produces a photocurrent of 35.9 mA/cm^2 at 0 V vs. RHE under simulated 1.5 AM G illumination.

Results and Discussion

Investigations of optical properties, structures, interfaces and surface morphologies

The fabrication process to make the $NiP_2/TiN/n^+p$-Si is summarized as follows (Figure 1a): First, a n^+p-Si buried PV junction was creating a degenerately phosphorous-doped surface on a p-type Si (100) wafer. A high-quality TiN/n^+p-Si structure with a sharp interface was created by pulsed laser deposition (PLD). 3 nm of nickel (Ni) was then thermally evaporated on top of TiN, followed by thermal phosphidation using red-P for synthesis of cubic-NiP_2 (See detailed procedure in Methods). A schematic description of the full photocathode and its absolute conduction band energies aids in understanding carrier transport in the device (Figure 1b). [49,50] To optimize the TiN film thickness and reveal its optical properties, varying thicknesses of TiN films were prepared on quartz substrates. Although the quartz substrate has different refractive index than Si, it allows unobstructed observation of the optical properties of TiN. In Figure S2, the spectra show a linear loss of transmittance as a function of thickness; films thicker than 6 nm reduce the transmittance to below 65%. When the deposited TiN layer is thinner than 4 nm, film conformality is an issue with random pinholes appearing, and therefore might not be able to serve as an adequate diffusion barrier (data not shown). At wavelengths above 380 nm, the measured transmittance of 4 nm TiN film on quartz is around 70%. However, to obtain the contribution only from absorption, we also measured the reflectance of 4 nm TiN on quartz and plotted it along with the absorptance and transmittance as a function of wavelength. (Figure S3). The absorptance of 4 nm TiN at a given wavelength ranges between 15 and 20%, with an estimated absorption coefficient of 5.2×10^5 cm^{-1} (at 500 nm). To further investigate the influence of the TiN film on total reflectance during operation, the reflectance of bare Si as well as 4 nm of TiN-coated Si were measured in dry (PV, in air) and wet conditions (PEC, with 1mm thick quartz window and 1 mm water layer) (Figure S4a). The TiN coating causes a very small change in total reflectance (1-2% decrease) in both dry and wet conditions. By contrast, there is a significant decrease in reflectance on going from dry to wet conditions for both bare and TiN-coated Si. As shown, this decreases 13-23% over the spectral range 400 -900 nm. These results indicate that the

quartz window and water layers substantially decreases the reflectance, which is well reproduced by calculations based on the Fresnel equations.[51] (Figure S4b) These opposing contributions offset one another and could possibly increase the light intensity that reaches Si when measured in the PEC configuration, as compared to bare Si PV alone.

Film properties and interfaces of the Si photoabsorber device were probed using cross-sectional scanning transmission electron microscopy (STEM), Rutherford backscattering

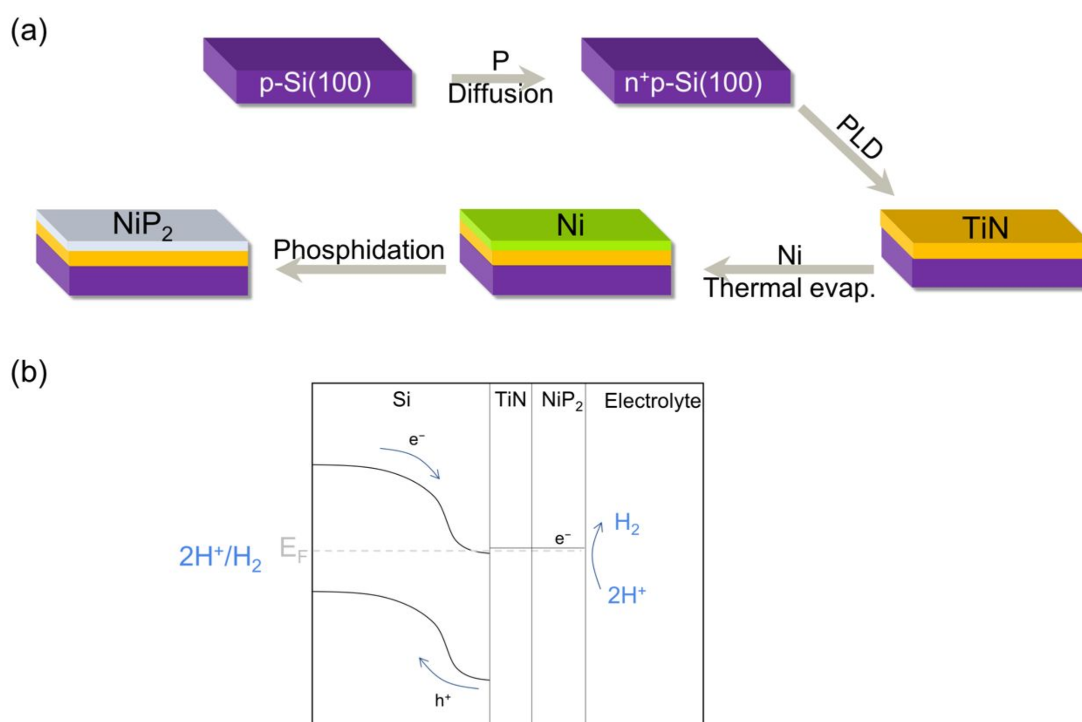

Figure 1. Schematic illustration of (a) NiP_2/TiN/n^+p-Si photocathode fabrication and (b) their band structure. (Band structure were reconstructed based on references 49, and 50)

spectrometry (RBS), and X-ray photoelectron spectroscopy (XPS, depth profile by Ar^+) (Figure 2). The cross-sectional STEM high-angle annular dark-field (HAADF) image of the as-deposited NiP_2/TiN/n^+p-Si sample verifies uniform deposition of TiN and NiP_2 with clear edges (Figure 2a). This confirms that the 4 nm thick TiN layer is indeed a good diffusion barrier for Si, allowing the formation of nickel phosphide without intermixing of Ni and Si during the high-temperature phosphidation. The high magnification STEM image (Figure 2b) reveals that the TiN layer appears to be overall polycrystalline, in-line with a previous report.[42] The high-resolution image of the NiP_2 top layer (Figure 2c) shows atomic-scale resolution

of NiP_2 growth along the (001) plane. The Fast Fourier Transformed (FFT) STEM image of the large NiP_2 grain (Figure 2c, upper inset) reveals the reciprocal space diffraction pattern. This pattern can be assigned to the [100] zone axis of cubic-NiP_2, thus demonstrating that synthesis formed nano-crystalline cubic-NiP_2. Other NiP_2 grains are matched with a [110] or [210] projection view, grown along the c-axis (normal to the surface). X-ray diffraction of a thicker film (>200 nm), indicates the bulk structure is polycrystalline cubic NiP_2 (Figure S5), suggesting that the as-prepared thin-film is partially oriented due to kinetic trapping of the polycrystalline product.

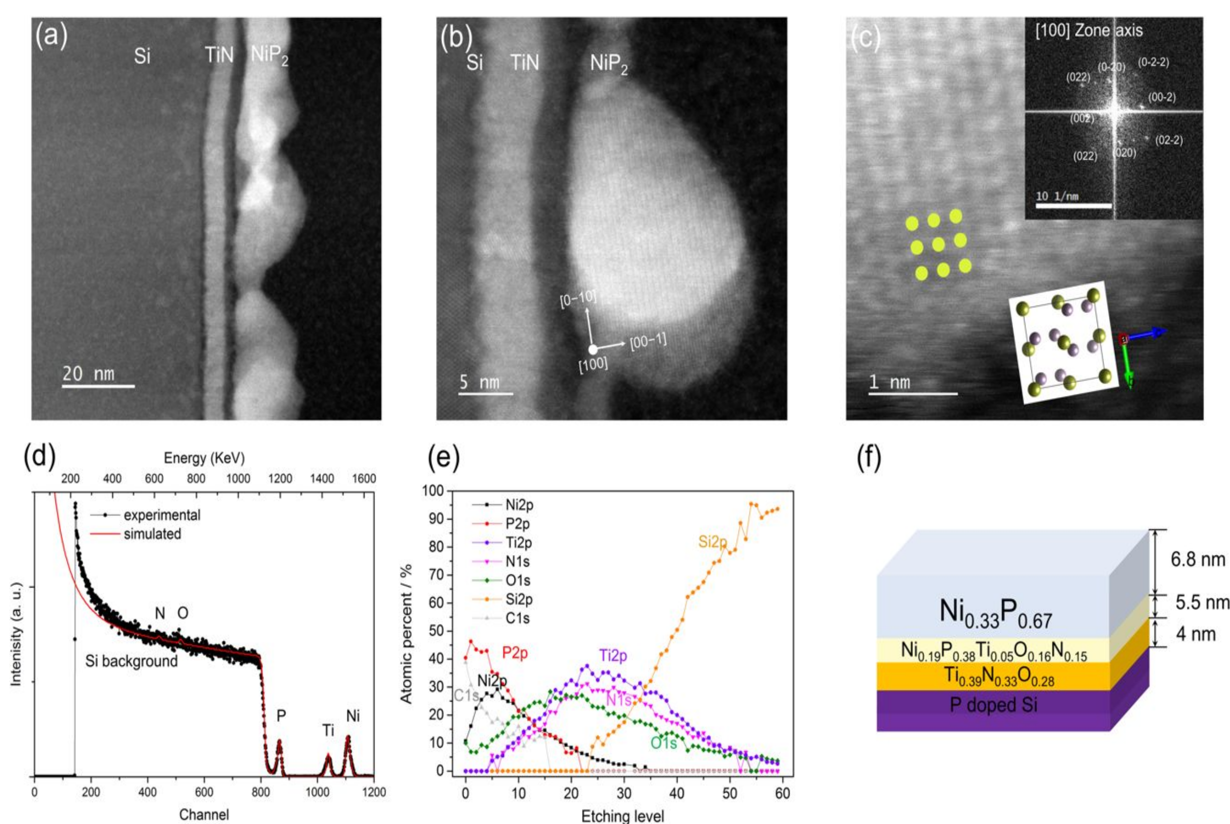

Figure 2. Structure and chemical analysis $NiP_2/TiN/n^+p$-Si photocathode. (a) Cross-sectional STEM high-angle annular dark-field (HAADF) low-magnification image of $NiP_2/TiN/n^+p$-Si, (b) high-magnification image of device interfaces and (c) atomic resolution image of cubic NiP_2. (Yellow is nickel, and purple is phosphorous) Inset shows FFT pattern of NiP_2 which is well matched with the [100] zone axis of cubic NiP_2. (d) RBS spectrum of $NiP_2/TiN/n^+p$-Si. (e) XPS depth profile of $NiP_2/TiN/n^+p$-Si (f) Thickness and chemical profiles of photocathode device based on RBS spectrum and XPS depth profile.

Both RBS and XPS were used to measure the thickness, the interfacial homogeneity, and the elemental composition as a function of depth of each layer (Figures 2d, 2e, and 2f). The

simulated RBS spectrum indicates that the composition of the top layer is $Ni_{0.33}P_{0.67}$ and contains 5.0×10^{16} atoms/cm^2, which corresponds to a thickness of 6.8 nm when calculated using the theoretical density. The thickness obtained from the RBS simulation is an average over the roughness of cubic NiP_2. The latter is evident in the cross-sectional TEM results (Figure 2a, b). Titanium nitride, in the next layer down, has an average composition and areal density corresponding to $Ti_{0.39}N_{0.33}O_{0.27}$ and 4.2×10^{16} atoms/cm^2. The estimated thickness is 4.0 nm (using the TiN density), similar to the cross-sectional TEM image result, which further shows it has uniform thickness (Figure 2a). The ~25% oxygen content of the TiN layer is

likely caused by the high temperature of the deposition in a less than perfect vacuum (4-7 × 10^{-4} Pa) and limited depth resolution. An interfacial region between TiN and NiP_2 can be seen in the cross sectional TEM image (Figure 2a), as the dark layer (low atomic mass) of thickness 2.2 nm (5.5 nm by RBS simulation). This layer has an average composition of $Ni_{0.2}P_{0.39}Ti_{0.05}O_{0.18}N_{0.2}$ and is formed during phosphidation, where Ni and P diffuse into the TiO_x-TiN layer.

XPS depth profiling was also used to investigate the TiN/Si interface (Figure 2e), which is seen in TEM to exhibit a clean boundary with the TiN layer. When performed just prior to deposition, the buffered oxide etchant cleaning steps remove silicon oxide from Si, that could increase the ohmic loss at this junction. [5249] XPS spectra of the Si core level as a function of sputtering time (Figure S6) proves that the Si does not contain an oxide impurity.

To evaluate the necessity of the TiN interfacial layer, we fabricated two control samples: 1) nickel phosphide thin-film directly on Si substrate (identical synthesis as Figure 1a, but with the TiN layer absent) and 2) replace the TiN interfacial layer with TiO_2. For the TiO_2 interfacial layer, a thin Ti layer (3 nm) was sputtered on clean Si prior to TiO_2 thin-film deposition (2.5 nm). This Ti layer consumes oxygen to prevent SiO_x formation at the TiO_2 and Si interface.[53] TiO_2 was deposited by PLD to allow direct comparison with TiN prepared the same way. The depth profile (Figure S1a) of phosphodized nickel film on Si without a

passivation layer shows that interdiffusion occurs and almost all of the Ni reacts with Si to form nickel silicide. A small amount of nickel phosphide is formed only at the very top layer. XPS core level spectra of the top surface (Figure S1b) shows the formation of a silicate layer (in addition to the nickel phosphide) that may be the surface oxide of the nickel silicide. In the case of the TiO_2 interfacial layer, the depth profile (Figure S7a) shows that nickel phosphide forms at the top, but it has slightly earlier onset of Si compared to that of TiN. When compared with a pristine TiO_2/Ti/Si interface (Figure S7b), the amount of oxygen in the TiO_2 layer is also decreased. These results indicate that diffusion of Si and O occurs and can form either $TiSi_x$ or SiO_x at the interface between TiO_2 and Si. These two control samples demonstrate that without a TiN interfacial layer, atomic diffusion occurs across the interface which can be detrimental for other performance metrics. The J-V performance of these half-cell devices is described in the PEC section.

To examine the surface morphology of the top catalyst layer of the TiN-protected photocathode, we used a helium ion microscope (HIM) for imaging (Figure 3a). [5451] This reveals uniform grains of cubic-NiP_2 with 20 – 30 nm width and 50 – 150 nm length of the individual grains with gaps in between grains. Atomic force microscope (AFM) imaging (Figure 3b) reveals additional vertical information.

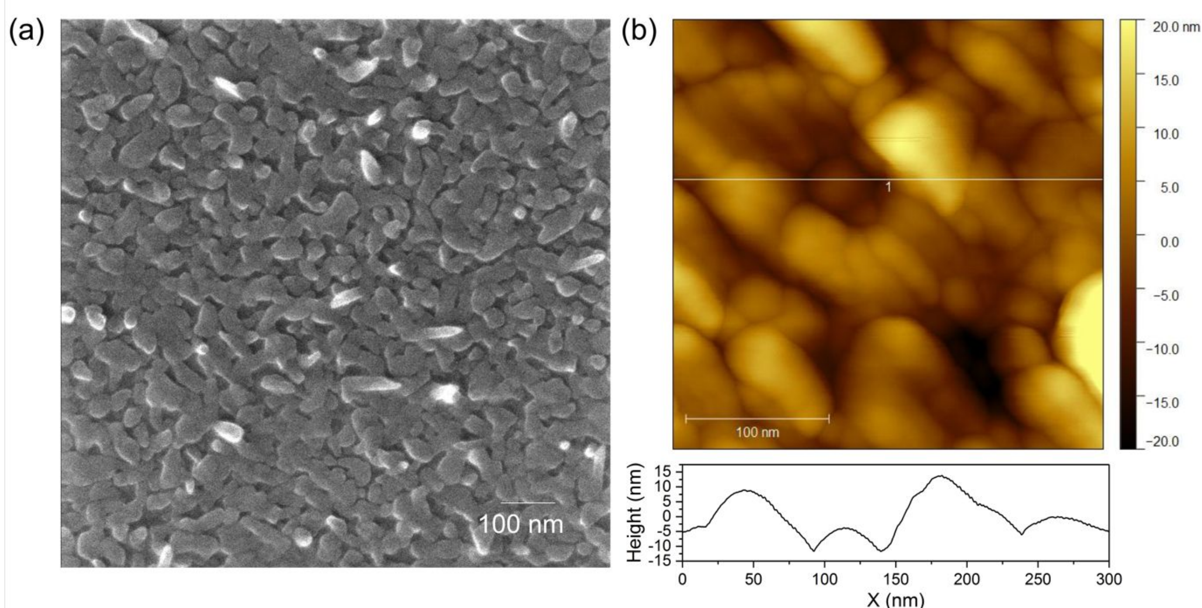

Figure 3. Morphologies of thin-film NiP_2 catalyst. (a) NiP_2 top layer of Helium ion microscope image and (b) AFM image. The bottom of AFM image indicates line profile (line 1). The film has uniform coating but having thickness variation (4-20 nm). Roughness is R_{rms} = 6.7 nm.

The AFM image and line profile indicate a thickness variation of the film from 4 nm to 20 nm. Both the HIM and AFM images indicate the conversion from Ni to c-NiP_2 causes the expansion of grains due to the density difference (Ni: 8.9 g/cm^3, c-NiP_2 4.89 g/cm^3), resulting in thickness variation by creating nanometer-scale gaps between grains. Topological information obtained from AFM is also helpful in understanding the true surface area of catalysts. The roughness factor from a larger area (5 × 5 μm) of the AFM profile (Figure S8a) is used to evaluate the turnover frequency (TOF) of the cubic-NiP_2 thin-film and compare it with other state-of-the-art catalysts below.

Thin-film cubic-NiP_2 catalyst HER activity

The HER activity of the thin-film cubic-NiP_2 catalyst was evaluated on n^+-Si (resistivity 0.005 ohm/cm – 10^{19-20} doping level, University Wafer) as the substrate (fabricated using the same procedure described above). All the electrochemical HER measurements are conducted using a three-electrode cell with 0.5 M sulfuric acid electrolyte. A boron-doped diamond counter electrode (Element Six, Da Beers) and mercury/mercury sulfate reference electrode (single junction Hg/Hg_2SO_4, PINE Instruments) were used. The reference electrode potential was calibrated against the reversible hydrogen electrode (RHE, Pt electrode at 1 atm H_2) before each measurement. To minimize contamination (by Cu^{2+} (from electrical leads) or Hg^{2+} (from the reference electrode)), we used anion exchange membrane (FKS, Fumatech) compartments on both reference and counter electrodes. Electrochemical impedance spectroscopy measurements were conducted to estimate the uncompensated solution resistance (Figure S9). To reduce the surface oxide that forms during air exposure, a negative bias was applied to achieve a current density of −10 mA/cm^2 for 10 min before the cyclic

voltammetry. Figure 4 shows IR-corrected and averaged cyclic voltammograms of cubic-NiP_2 thin-film catalyst, c-NiP_2/TiN/n^+-Si and a benchmark (polycrystalline Pt foil) reveals that the potential required to obtain −10 mA/cm^2 is 167 mV (vs. RHE) and 31 mV for thin-film cubic-NiP_2 catalyst and the benchmark, respectively. The cubic-NiP_2 thin-film catalyst generated H_2 with 100% Faradaic efficiency (Figure S10). The applied potential plotted as a function of the logarithm of the current density derived from linear sweep voltammetry (Figure S11) indicates a Tafel slope and exchange current density of 41 mV/dec, and 3.0×10^{-6} A/cm$^2_{geo}$, respectively. In order to minimize capacitive charging effects on the Tafel slope, we also measured the steady-state current during chronoamperometry (CA) at various fixed potentials, which gave a Tafel slope of 40 mV/dec (Figure S11). The two methods give the same result indicating there is negligible capacitive charging of the thin-film cubic-NiP_2, presumably due to its low roughness factor. The obtained Tafel slope is 20-32% lower than both thick (51 mV/dec) and thin-film (61 mV/dec) polycrystalline cubic-NiP_2 electrocatalysts reported by others. [33,55] This value of the Tafel slope indicates that the Volmer-Heyrovsky mechanism is the likely rate-determining step for HER. [56]

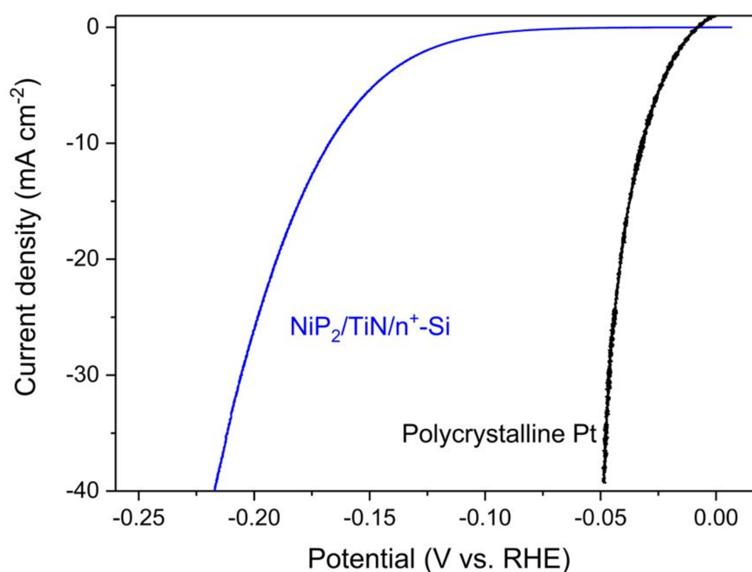

Figure 4. Electrochemical activity of thin-film NiP_2 catalyst. IR-corrected averaged cyclic voltammograms (CV) of the NiP_2 thin-film catalyst (NiP_2/TiN/n^+-Si, blue) and polycrystalline Pt (black) for benchmark.

This lower Tafel slope indicates that our thin-film catalyst method produces a better HER efficiency using NiP_2 than other reported methods so far. For comparison, TMP thin-film catalysts (< 50 nm), such as CoP and Ni_2P on Si substrate have overpotentials of 202 mV and 240 mV (vs. RHE) at a current density of −10 mA/cm^2_{geo} based on the geometric surface area, while their Tafel slope is 60 mV/dec and 66 mV/dec, respectively. [31,3428,31] This comparison shows that our method for producing cubic-NiP_2 thin-film catalyst on TiN/Si has the highest reported HER activity amongst all thin-film TMP catalysts reported thus far, to our knowledge.

To determine the turnover frequency (TOF) and allow direct comparison of the intrinsic activity of catalysts, the number of active sites is required. Here, we estimated the TOF by electrochemical surface area (ECSA), using the method of Kibsgaard, *et al.* (Figure S8b). [3027] Application of this method yields a TOF of 0.41 H_2 $site^{-1}$ s^{-1} for cubic-NiP_2 thin-films at E= −100mV vs RHE (see detailed calculation in electronic supplementary information). This compares very well with TOFs from other studies of powder-based TMP catalysts, [22,30] summarized in Figure S12. For example, the TOF of these thin-films is 1-order of magnitude smaller than that of Ni_5P_4 nanocrystalline-micron particles (3.5 s^{-1} TOF; the best known HER catalyst after Pt) and on par with $Fe_{0.5}Co_{0.5}P$ (0.19 s^{-1} TOF). [22,30]

We also estimated the surface area using an AFM image-derived roughness factor (Figure S8a), as demonstrated by Hellestern, *et al.* for a thin-film TMP catalyst. [31] The obtained roughness factor of thin-film NiP_2 is 1.08 cm^2_{ECSA}/cm^2_{geo}, assuming an average Ni and P surface coverage (i.e. assuming both are active sites) a TOF of 1.04 H_2 $site^{-1}$ s^{-1} is obtained. This estimate points to cubic-NiP_2 as the second most active TMP catalyst reported. This difference could be due to either the ECSA estimate exaggerating the surface area because of a pseudo-capacitance contribution, or conversely, the AFM surface roughness under estimating the true surface area due to small porosity not resolved by AFM (the surface between the agglomerated particles, as seen by STEM in Figure 2b).

The low Tafel slope, and exceptional TOF of our cubic-NiP_2 thin-film catalyst, may be attributed to the preferred facet orientation of NiP_2 (001), revealed in the STEM cross-section. The assumption is that this preferentially exposes a higher activity facet compared to a random distribution of orientations (polycrystalline). Conversely, other factors such as a limited mass transport and inaccurate ECSA measurement for thicker films may influence the accuracy of the TOF estimate.

Photoelectrochemical activity

To estimate the maximum saturation photocurrent and photovoltage of NiP_2/TiN/n^+p-Si, we first probed the photovoltaic properties (short circuit current density, J_{sc} and open-circuit potential, V_{oc}) of bare n^+p-Si (Figure S13). Note that the PV properties are lower (J_{sc} ~ 16.3 mA/cm^2 and V_{oc} ~ 525 mV) than a fully optimized commercial Si solar cell (J_{sc} ~ 40 mA/cm^2 and V_{oc} ~ 727 mV) due to the absence of a pp^+ junction, and top anti-reflective and bottom reflective coatings. [57] To determine the influence of the NiP_2 and TiN layers and the alternative TiO_2 interfacial layer, 4 devices were prepared and compared: TiN/n^+p-Si, NiP_x/$NiSi_y$/n^+p-Si (same as Figure S1), NiP_2/TiO_2/Ti/n^+p-Si (same as Figure S7a), and Pt/TiN/n^+p-Si (benchmark). The benchmark device was fabricated by drop-casting and electroreduction to form nanoparticles of Pt on TiN/n^+p-Si, similar to the method described Chorkendorff and co-workers. [25] This benchmark Pt catalyst should give idealized photoelectrochemical HER activity and uniform, measurable, light loss.

Non-IR corrected J-V curves for the prepared devices are shown in Figure 5a for simulated AM 1.5 G illumination. For TiN/n^+p-Si, a photocurrent density of −0.5 mA/cm$^2_{geo}$ (we define V_{onset} as the potential needed to produce this current) and −10 mA/cm$^2_{geo}$ were reached at –400 mV and –700 mV vs RHE, respectively. The obtained saturated photocurrent density (J_{sat}) (~ −17.6 mA/cm$^2_{geo}$) is slightly higher than the silicon PV cell alone (J_{sc} ~ −16.3

mA/cm^2_{geo}) as expected from the optical performance of the TiN thin-film on Si in PEC configuration. (Figure S13). For the $NiP_x/NiSi_y$/ n^+p-Si, the J-V curve (Figure 5a) shifts negative by 175 mV at −10 mA/cm^2_{geo} compared to that of TiN/ n^+p-Si. This shift clearly shows that the absence of TiN results in substantial loss of electrochemical HER performance. This can be attributed to the formation of $NiSi_y$ on the surface as seen by XPS (Figure S1), which is not catalytically active for HER.

In the case of NiP_2/TiN/n^+p-Si photocathode, the J-V curve shifts positive (by 910 mV) due to the high HER activity of the cubic NiP_2 thin-film when protected by the TiN interlayer and reaches current densities of −0.5 mA/cm^2_{geo} (V_{onset}) and −10 mA/cm^2_{geo} at 399 mV and 254 mV vs. RHE, respectively. This compares to the benchmark Pt/TiN/n^+p-Si, of only 100 mV and 150 mV at these current densities, respectively. Using the latter photocathode as the reference electrode potential allows direct extraction of the purely electrochemical overpotential (i.e. disregarding the photovoltage). Comparing NiP_2/TiO_2/Ti/n^+p-Si to the NiP_2/TiN/n^+p-Si photocathode, both a significantly lower HER activity (170 mV vs. RHE at −10 mA/cm^2) and photocurrent density (13.9 mA/cm^2) are observed. This result is consistent with the XPS depth profiles (Figure S7), showing the diffusion of Si and O to form a high resistance SiO_x and a highly absorptive metallic $TiSi_x$ at interfaces. This outcome reinforces the advantage of using TiN vs. TiO_2 as a protection layer to prevent both the deleterious effects from oxygen and silicon diffusion.

Figures 5b-c show the separate direct comparison of the photovoltage for NiP_2/TiN/n^+p-Si and benchmark photocathodes. The photovoltage of the Pt/TiN/n^+p-Si benchmark (532 mV, Figure 5b) is similar to V_{oc} of the PV cell, measured in the absence of electrolyte interfaces and catalysis (see Figure S13).

Although cubic-NiP_2 has metallic properties (conductivity and opacity), NiP_2/TiN/n^+p-Si (Figure 5c) shows only a 3% loss of photovoltage (512 mV) due to the cubic-NiP_2 layer. This low value is attributed to the layer thinness (4-20 nm) with nanometer gaps and a clean interface

(no nickel silicide). This result agrees with the J-V curves (Figure 5a), which show almost the same J_{sat} (−18.5 mA/cm$^2_{geo}$) of the NiP_2/TiN/n$^+$p-Si as the benchmark Pt/TiN/n$^+$p-Si photocathode.

The above results clearly demonstrate that the combined cubic-NiP_2/TiN thin-film layers have better or comparable catalytic activity than other reported thin-film TMP catalysts when used on photocathodes, and maximal photocurrent density J_{sat} (>100% vs J_{sc} of PV cell, and 100% vs J_{sat} of the benchmark Pt/TiN/n$^+$p-Si photoelectrode). To the best of our knowledge, this is the first report that shows near maximum saturated photocurrent density, while maintaining excellent catalytic activity in a TMP thin-film catalyst photocathode. In previous reports, using an optimized thickness of CoPS as an HER catalyst ~ 72% J_{sat} was achieved compared to a Pt/n$^+$p-Si benchmark photoelectrode, while an optimized thickness of CoP achieved ~ 74 % of J_{sat} of the Pt/n$^+$p-Si benchmark. [31,58] At wavelengths >550 nm, incident photon-to-current efficiency (IPCE) reveals that NiP_2/TiN/n$^+$p-Si is > 50% efficient (Figure S14). Loss of efficiency at wavelengths below 500 nm is attributed to light absorption in the cubic-NiP_2/TiN thin-film layers, which causes recombination and thus does not contribute to the photovoltage and J_{sat}, in agreement with observations in literature for surface protected n$^+$p-Si photoelectrodes. [31]

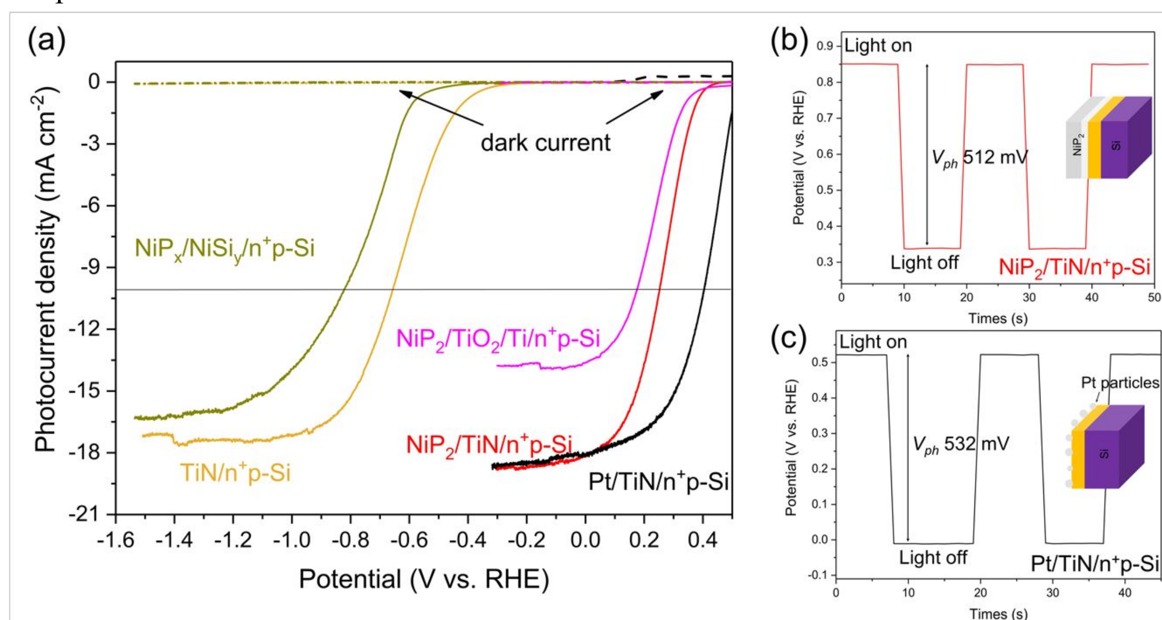

Figure 5. Photoelectrochemical performance at simulated AM 1.5 G solar illumination (a) non-IR-corrected *J-V* curve of $NiP_x/NiSi_y/n^+p$-Si, TiN/n^+p-Si, $NiP_2/TiO_2/Ti/n^+p$-Si, $NiP_2/TiN/n^+p$-Si, and $Pt/TiN/n^+p$-Si exposed on simulated solar illumination and dark in 0.5 M H_2SO_4 (scan rate: 10 mV/s). For driving a current density of -10 mA/cm^2, $NiP_2/TiN/n^+p$-Si requires 150 mV overpotential compared to $Pt/TiN/n^+p$-Si. Open-circuit potential measurement under simulated AM 1.5 G illumination and dark for (b) $NiP_2/TiN/n^+p$-Si and (c) benchmark $Pt/TiN/n^+p$-Si.

Photoelectrochemical stability

To demonstrate the photoelectrochemical stability of the device, chronoamperometry (CA) was conducted under simulated 1-sun illumination in 0.5 M H_2SO_4 at 0 applied V vs. RHE (Figure 6a). The photocathode maintains a stable H_2 evolution photocurrent (standard deviation, $A_0 \pm 10\%$) without failure for at least 125 hours in acid, which was the maximal duration of our experiments. No long-term degradation on this time scale was detectable. This contrasts with previous reports of other thin-film catalysts which dissolved or delaminated during operation, allowing for corrosion of any newly uncovered photoabsorber. [59,60] We investigated the chemical state of the electrode surface by XPS (2p core levels see Figure 6b-d) of our photocathode over time. For the as-prepared sample, the binding energy of $Ni2p_{3/2}$ is 854.6 eV, shifted to higher energies compared to standard nickel phosphides (853.2 eV) reported in NIST or other literature. [34,61] This shift likely occurred due to surface oxidation with the inevitable air exposure between electrolysis and analysis. The major P peak ($2p_{3/2}$ core level) occurs at 129.3 eV close to elemental P, as well as a minor peak at 133.2 eV in the P-O (phosphate) region. For Ti, a low signal-to-noise intensity was observed for the Ti 2p core level, as expected due to conformal coverage of the NiP_2 top layer. As expected, no Si was detected which is attributed to the absence of Si diffusion in the upper layers and the NiP_2/TiN thickness being far beyond the electron escape depth ($<$ 3 nm). [62]

XPS studies at 26 hours of continuous photoelectrolytic operation (Figure 6c), reveals P, Si and Ti core level unchanged, but now a chemically reduced Ni state (violet) appears, which is attributed to the catalytically active state of the nickel phosphides during electrolytic HER. [13,54,55] This reduction occurs in parallel with partial removal of the surface P-O

(orange). After 125 hours of operation (Figure 6d), the surface of oxides of both Ni and P were further reduced, but minor peaks for silicon oxide and titanium oxide were now detected at the top surface (Figure S15). In order to verify the source of these elements, gentle sputtering (60 s, 1000 eV Ar^+) was conducted to etch the surface layer, followed by XPS measurement. The sputter cleaning reveals that both silicon and titanium oxides were removed, hence they are found only at the top surface with the electrolyte interface (Figure

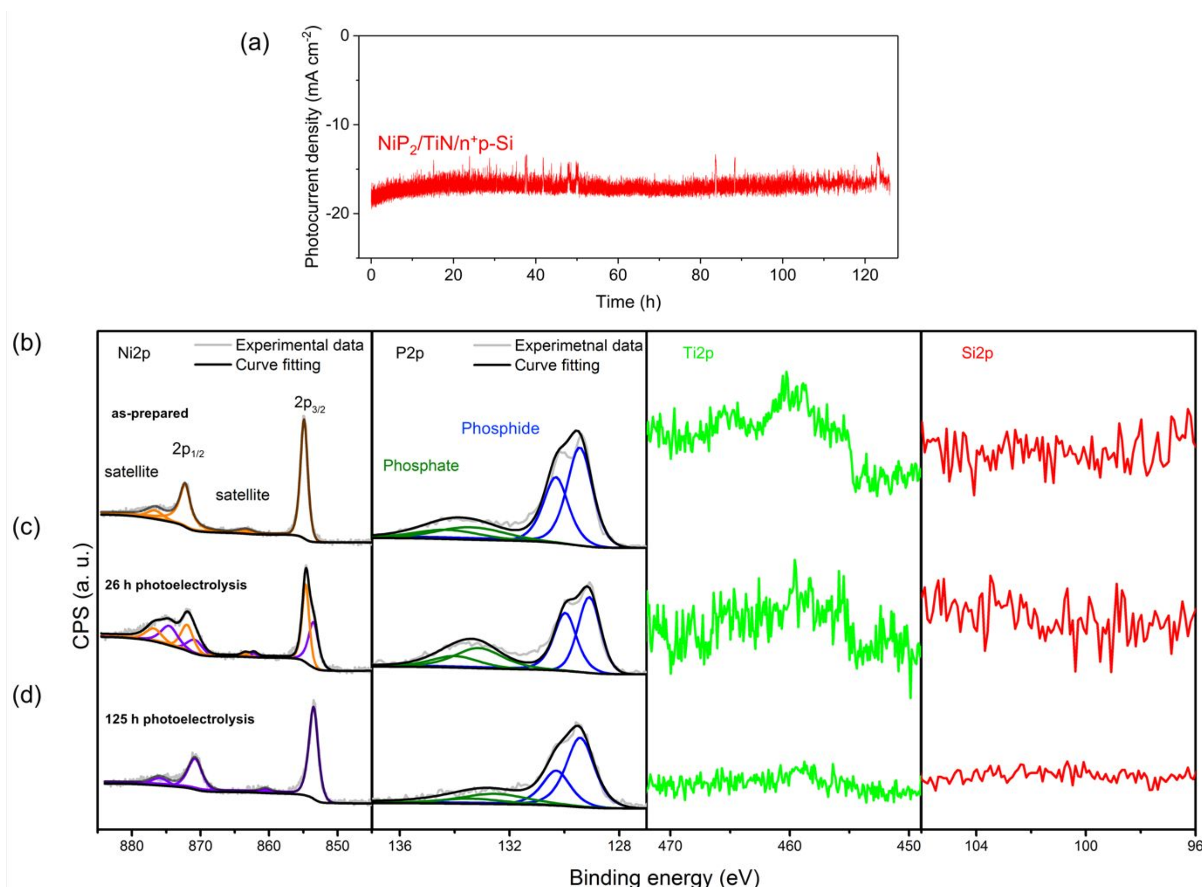

Figure 6. Photoelectrochemical stability of NiP_2/TiN/n$^+$p-Si. (a) chronoamperometry (CA) measurement of NiP_2/TiN/n$^+$p-Si photocathode for 125 h continuous illumination at 0 V vs. RHE in 0.5 M H_2SO_4. Time-dependent XPS measurement for (b)as-prepared, (c) after 26 h and (d) after 125h photoelectrolysis of NiP_2/TiN/n$^+$p-Si samples. Ni2p and P2p core level shows experimental data (grey) and fitting envelope (black line), and peak fits corresponding to surface oxidized Ni (orange), metallic Ni (violet), metallic P (blue), and phosphate (green). For Ti2p (light green) and Si2p (red), no noticeable signals have been detected.

6d). The surface silicon oxide contamination likely came from the fracture of the Si substrate during disassembly of the epoxy-sealed electrode. Similarly, titanium oxide came from the nanoparticulate TiO_2 additive in the epoxy (Loctite Hysol 1C) required to properly mask the illumination area. [63]

Together these time-dependent CA and XPS results demonstrate that the cubic-NiP_2/TiN thin-film layers do not degrade or delaminate during 125 h operation. During photoelectrolysis the catalyst undergoes electrochemical transformation consistent with the expected redox activation for HER. [22,64] We conclude that the materials, the interfaces and the processing methods provide excellent stability during extended photoelectrochemical turnover.

Applicability of thin-film cubic-NiP_2/TiN layers

While a highly efficient thin-film electrocatalyst should decrease the kinetic barrier for HER with negligible parasitic light absorption, overall photoelectrochemical performance often times relies strongly on the photoabsorber's properties. To enhance the photoelectrochemical performance and demonstrate the versatility of the c-NiP_2/TiN catalyst/protection layers, we applied these to a commercially available crystalline Si solar cell. This allows understanding of the correlation between the performance of the cubic-NiP_2/TiN thin-film layers (catalytic activity and negligible light absorption) and the properties of an independently benchmarked and readily available photoabsorber.

In contrast to the in-house fabricated n^+p-Si photoabsorber, the single-crystal Si solar cell (sc-Si) is covered with several front and back antireflective coatings, reflective internal layers and digitated silver metal contacts. [6562] Before applying the catalyst/protection layers to the sc-Si solar cell, sequential wet-etching steps are required to uncover the pristine Si surface (see Experimental details). The HIM image of the etched sc-Si solar cell (e-Si) shows the micro-pyramidal morphology of Si which is commonly used for the high efficiency Si solar cell (Figure S16a). [65] Elemental XPS analysis demonstrates the presence of only Si (residual O from the native oxide and adventitious C) and the absence of other expected surface element impurities (Ag, Al) (Figure S16c-d), consistent with the successful removal of the surface layers (Figure S16b). Standard PV properties of sc-Si, e-Si, and n^+p-Si in the absence

of electrolyte are compared in Figure S17 and summarized in Table S1. These results reveal that commercial sc-Si and e-Si produce doubled J_{sc} compared to that of the in-house produced n^+p-Si. The e-Si sample has a ~10% lower J_{sc} than sc-Si, due to the removal of the surface coatings. In contrast, the V_{oc} is not substantially different between the in-house fabricated n^+p-Si and the e-Si solar cell, while the sc-Si does show a slight improvement over the e-Si. The

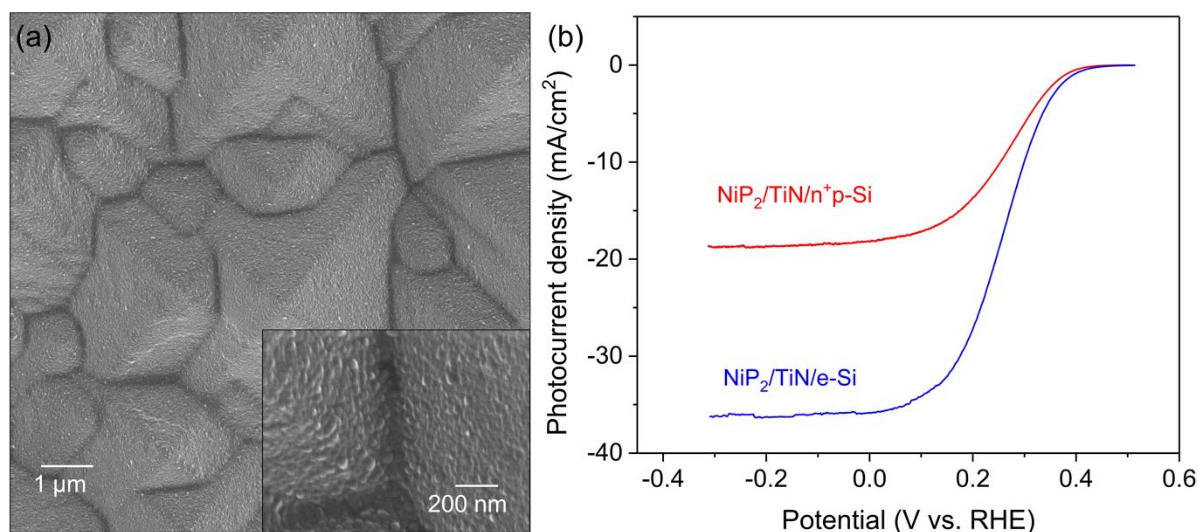

Figure 7. (a) Helium ion microscope image of NiP_2 surface obtained from commercial micropyramid Si solar cell substrate (NiP_2/TiN/e-Si). High-magnification image of inset shows uniform coverage of NiP_2 grains. (b) Photoelectrochemical performance (Non IR-corrected J-V curve) of NiP_2/TiN/n^+p-Si and NiP_2/TiN/e-Si exposed on simulated 1.5 AM G illumination in 0.5 M H_2SO_4 (Scan rate: 10 mA/cm^2).

most obvious difference between the e-Si and sc-Si is the decreased fill factor, which is attributed to the removal of the top anti-reflective coatings and digitated metal silver contact. Cubic-NiP_2/TiN thin-film layers were then fabricated on the e-Si substrate using the same method described above. A HIM image of this junction (Figure 7a) shows the same Si micropyramidal structure as on the pristine e-Si with no additional morphologies, indicating uniform coverage by the catalyst/protection layers. A high magnification image (Figure 7a, inset) reveals NiP_2 grain sizes in the interval of 20 – 40 nm, similar to that of the in-house junction, NiP_2/TiN/n^+p-Si (Figure 3a). Comparing the non-IR corrected photoelectrochemical J-V curve of NiP_2/TiN/e-Si (Figure 7b), it reaches current densities of −0.5 mA/cm^2_{geo} (V_{onset}) and −10 mA/cm^2_{geo} at 405 mV and 313 mV vs. RHE, respectively. Between 0 and -0.4 V vs.

RHE a constant photocurrent density is achieved of mean value −36.3 mA/cm^2 (J_{sat}) with 100% Faradaic efficiency (Figure S10). J_{sat} of NiP_2/TiN/e-Si is two-times higher than the J_{sat} using the in-house fabricated PV junction, NiP_2/TiN/n^+p-Si, at the given potential; indicating that the c-NiP_2/TiN catalyst/protection layers can effectively be applied to PV-optimized commercial grade solar cells without losses in photoabsorber properties. When the IPCE is measured at 0 V vs. RHE (Figure S14), it is over 70% at wavelengths above 500 nm. Comparing the PV (electrolyte-free) properties of the bare e-Si substrate to those of the NiP_2/TiN/e-Si, J_{sat} is slightly increased and 98% of photovoltage is retained (Figure S18), analogous to the observations for the n^+p-Si substrate. This clearly demonstrates that our newly developed cubic-NiP_2/TiN thin-film catalyst/protection layers do not compromise the photoelectrochemical properties and is directly applicable to high efficiency, commercial-grade single crystal Si photoabsorbers.

Conclusion

We have developed a successful fabrication route to nano-crystalline thin-films of cubic-NiP_2 on a TiN-protected Si photocathode that allows efficient PEC water splitting using low cost materials. The elemental and structural analysis conducted by STEM, RBS, and XPS demonstrates the importance of the TiN interfacial layer as a necessary component to inhibit elemental diffusion during photoelectrode fabrication. The specific advantages of TiN are demonstrated relative to a commonly used TiO_2 interfacial layer. The latter underperforms relative to TiN because it is incapable of preventing atomic diffusion during the high temperature synthesis. Cross-sectional STEM analysis identified partially oriented NiP_2 along the (001) plane, which may contribute to its superior HER performance. HER activity when normalized to two independent surface area estimates indicates excellent TOF (0.41 to 1.04 H_2 site^{-1} s^{-1}) for the NiP_2 thin-film. Photoelectrochemical studies confirm that the saturated photocurrent density is not compromised by the metallic NiP_2 and TiN layers, while

maintaining high catalytic activity for HER. The corrosion resistance of cubic-NiP_2/TiN thin-film layers demonstrates stable activity for over 125 hours without deleterious changes to the performance during the test. When these catalyst/protection layers are applied to a commercial-grade high efficiency Si photoabsorber, it retains high photoelectrochemical performance, thereby showing the applicability of this strategy to highly-engineered commercial solar cell. The facile implementation of the cubic-NiP_2/TiN thin-film catalyst/protection layers opens an opportunity to investigate their implementation onto other highly engineered photoabsorbers (such as multijunction Si, and high-efficiency III-V semiconductors). In conclusion, our work illustrates the opportunity to improve long term operation of photoelectrochemical systems using earth-abundant materials. Precious metals are not necessary, neither for catalysis nor durability of the electrolyte/catalyst/photoabsorber interfaces. These advances bring energy conversion from sunlight into fuels closer to reality.

Experimental methods

Physical characterizations: A cross-sectional STEM sample was prepared by an *in-situ* lift-out method using FEI Helios Nanolab 600 dual beam SEM/FIB at Brookhaven National Laboratory. Amorphous carbon was chosen for the first sacrificial layer. Gallium ions with a fairly low acceleration of 2 KeV were used for final thinning to eliminate surface amorphization and Ga contamination. High angle annular dark field (HAADF) imaging was performed on a Nion UltraSTEM at Rutgers with an accelerating voltage of 60 kV and collecting signal angles above 145 mrad. The microscope is equipped with an aberration corrector, which enables the spatial resolution close to 1 Å. For XPS, a Thermo K-Alpha spectrometer was used with a flood gun for charge compensation. Spectra were calibrated against adventitious carbon (284.8 eV). For time-dependent XPS measurements, X-rays with a spot size of 200 μm were focused on each sample. For depth profiling, sputtering with a 3.5 mm diameter (much larger than the imaged area) was achieved by Ar sputtering at 1 keV. An

X-ray beam with a 35 μm diameter was used every 30 s until only Si was observed indicating that the film was fully etched and the silicon substrate was exposed. Helium ion microscopy was carried out on an Orion Plus Helium Ion Microscope (Carl Zeiss) operating at a 30 kV acceleration voltage and an ion beam current around 1 pA. Atomic force microscopy (AFM) images were taken using a Park Systems (Suwon, Korea) NX-10 with a Nanosensor (Neuchatel, Switzerland) PPP-NCHR tip in non-contact mode at room temperature. Rutherford backscattering spectrometry (RBS) was performed using a 2 MeV He^{2+} beam source from the Rutgers University tandem accelerator. The incident beam was normal to the surface and the backscattered He ions were collected by silicon detectors at a 163° back-scattering angle. Data fitting and modeling were accomplished using the SIMNRA 6.06 software package. The theoretical densities were taken from the appropriate crystal structures (NiP_2 PDF 01-073-0436, TiN 01-087-0633 and $Ni_3(PO_4)_2$ 01-072-3977).

Electrode assembly: The method for electrode assembly was adopted from elsewhere.[66] An electrical contact of the prepared electrodes was made on the back side of the silicon substrate scoring in the presence of a Ga-In eutectic (99.99% Aldrich). A copper or zirconium wire was attached to the eutectic with conductive silver paint (SPI supplies). The wire was then inserted into a Pyrex glass tube. The back side of the electrode were finally sealed with a mixture of epoxy resin (Loctite Hysol 1C) and TiO_2 nanoparticle (p25, Evonik). Electrode areas were measured with a digital photograph and ImageJ analysis. Typical electrode areas ranged between 0.1 – 0.3 cm^2.

Photoelectrochemical measurements: Photoelectrochemical measurements were performed in a custom built three-electrode glass cell in H_2 purged 0.5 M H_2SO_4 using a Bio-logic potentiostat (SP-150). The working electrodes were illuminated by simulated 1.5 AM G illumination (AM1.5G, 100 mW/cm^2) supplied by a 75 W Xe arc lamp (ORIEL) through a quartz viewport in the cell. The photoelectrode (working electrode) locates 5 mm away from the quartz viewport. For counter and reference electrode, a boron-doped diamond electrode

(Element Six, Da Beers) and mercury/mercury sulfate reference electrode (single junction Hg/Hg_2SO_4, PINE Instruments) were used. We used anion exchange membrane (FKS, Fumatech) compartments (membrane attached quartz tubes) on both reference and counter electrodes to minimize the cross-contamination. The reference electrode potential was calibrated against the reversible hydrogen electrode (RHE, Pt electrode at 1 atm. H_2) before each measurement. All J-V curves are obtained by averaged cyclic voltammograms at the scan rate of 10 mV/s.

IPCE measurement: Measurements were performed using monochromated light from a 1000 W Xe arc lamp (Oriel) light source. The wavelength of light was selected by a monochromator (Horiba) and ranged from 400 nm to 900 nm at 50 nm intervals except for 840 nm which replaced 850 nm due to a spike in the light source intensity. The working electrode was held at 0.0 V vs. RHE using Biologic potentiostat and the measured photocurrent was derived as the difference between the dark and illuminated current values.

Author Contributions

S. H. synthesized the samples and conducted the XPS, XRD, and photo/electrochemical measurement. S. H. P. prepared and optimized the buried junction n^+p-Si and conducted the photoelectrochemical measurement. H. Y. conducted the cross-sectional STEM. M. L. performed the AFM. V. M. performed the HIM. K. U. D. C. assisted with the faradaic efficiency test. V. A. conducted thicker Ni deposition. S. H., S. H. P., A. B. L., M. G., E. G., and G. C. D. designed the experiments. All authors contributed to writing the manuscript.

Acknowledgements

This work was supported by a joint DOE-EERE (energy Efficiency and Renewable Energy)/NSF-CBET (Chemical, Bioengineering, Environmental, and Transport systems) award number 1433492 and continuation award from DOE-EERE number DE - EE0008083. This research used resources of the Center for Functional Nanomaterials, which is a U.S. DOE Office of Science Facility, at Brookhaven National Laboratory under Contract No. DE-SC0012704. We thank R. Thorpe for measuring RBS spectra, and J. Tracey, and D. M. O'Carroll for helping with reflectance measurements.

References

1 M. Z. Jacobson, W. G. Colella and D. M. Golden, *Science*, 2005, **308**, 1901–1905.
2 K. Christopher and R. Dimitrios, *Energy Environ. Sci.*, 2012, **5**, 6640–6651.
3 N. S. Lewis and D. G. Nocera, *PNAS*, 2006, **103**, 15729–15735.
4 A. J. Bard and M. A. Fox, *Acc. Chem. Res.*, 1995, 141–145.
5 A. Fujishima and K. Honda, *Nature*, 1972.
6 A. B. Laursen, S. Kegnæs, S. Dahl and I. Chorkendorff, *Energy Environ. Sci.*, 2012, **5**, 5577–5591.
7 M. S. Prévot and K. Sivula, *J. Phys. Chem. C*, 2013, **117**, 17879–17893.
8 J. L. Young, M. A. Steiner, H. Döscher, R. M. France, J. A. Turner and T. G. Deutsch, *Nature Energy*, 2017, **2**, 17028.
9 W.-H. Cheng, M. H. Richter, M. M. May, J. Ohlmann, D. Lackner, F. Dimroth, T. Hannappel, H. A. Atwater and H. J. Lewerenz, *ACS Energy Letters*, 2018, **3**, 1795–1800.
10 B. Turan, J.-P. Becker, F. Urbain, F. Finger, U. Rau and S. Haas, *Nat Comms*, 2016, **7**, 12681.
11 S. Nordmann, B. Berghoff, A. Hessel, B. Zielinsk, J. John, S. Starschich and J. Knoch, *Sol. Energy Mater. Sol. Cells*, 2019, **191**, 422–426.
12 F. Urbain, P. Tang, N. M. Carretero, T. Andreu, L. G. Gerling, C. Voz, J. Arbiol and J. R. Morante, *Energy Environ. Sci.*, 2017, **10**, 2256–2266.
13 F. Urbain, V. Smirnov, J.-P. Becker, U. Rau, J. Ziegler, B. Kaiser, W. Jaegermann and F. Finger, *Sol. Energy Mater. Sol. Cells*, 2015, **140**, 275–280.
14 J. Jia, L. C. Seitz, J. D. Benck, Y. Huo, Y. Chen, J. W. D. Ng, T. Bilir, J. S. Harris and T. F. Jaramillo, *Nat Comms*, 2016, **7**, 13237.
15 S. Hu, M. R. Shaner, J. A. Beardslee, M. Lichterman, B. S. Brunschwig and N. S. Lewis, *Science*, 2014, **344**, 1005–1009.
16 B. Seger, S. D. Tilley, T. Pedersen, P. C. K. Vesborg, O. Hansen, M. Grätzel and I. Chorkendorff, *J. Mater. Chem. A*, 2013, **1**, 15089–15094.
17 R. Fan, J. Mao, Z. Yin, J. Jie, W. Dong, L. Fang, F. Zheng and M. Shen, *ACS Appl. Mater. Interfaces*, 2017, **9**, 6123–6129.
18 R. J. Britto, J. D. Benck, J. L. Young, C. Hahn, T. G. Deutsch and T. F. Jaramillo, *J. Phys. Chem. Lett.*, 2016, **7**, 2044–2049.

19 F. Urbain, V. Smirnov, J.-P. Becker, A. Lambertz, F. Yang, J. Ziegler, B. Kaiser, W. Jaegermann, U. Rau and F. Finger, *Energy Environ. Sci.*, 2016, **9**, 145–154.
20 F. Urbain, V. Smirnov, J.-P. Becker and F. Finger, *ACS Omega*, 2016, **1**, 832–836.
21 D. Voiry, M. Salehi, R. Silva, T. Fujita, M. Chen, T. Asefa, V. B. Shenoy, G. Eda and M. Chhowalla, *Nano Lett.*, 2013, **13**, 6222–6227.
22 A. B. Laursen, K. R. Patraju, M. J. Whitaker, M. Retuerto, T. Sarkar, N. Yao, K. V. Ramanujachary, M. Greenblatt and G. C. Dismukes, *Energy Environ. Sci.*, 2015, **8**, 1027–1034.
23 X. Wang, Y. V. Kolen'ko, X. Q. Bao, K. Kovnir and L. Liu, *Angew. Chem. Int. Ed. Engl.*, 2015, **54**, 8188–8192.
24 B. Seger, T. Pedersen, A. B. Laursen, P. C. K. Vesborg, O. Hansen and I. Chorkendorff, *J. Am. Chem. Soc.*, 2013, **135**, 1057–1064.
25 B. Seger, A. B. Laursen, P. C. K. Vesborg, T. Pedersen, O. Hansen, S. Dahl and I. Chorkendorff, *Angew. Chem. Int. Ed.*, 2012, **51**, 9128–9131.
26 Y. Yan, B. Xia, Z. Xu and X. Wang, *ACS Catal.*, 2014, **4**, 1693–1705.
27 Z. Huang, Z. Chen, Z. Chen, C. Lv, H. Meng and C. Zhang, *ACS Nano*, 2014, **8**, 8121–8129.
28 X. Q. Bao, M. F. Cerqueira, P. Alpuim and L. Liu, *Chem. Commun.*, 2015, **51**, 10742–10745.
29 Z. W. Seh, J. Kibsgaard, C. F. Dickens, I. Chorkendorff, J. K. Nørskov and T. F. Jaramillo, *Science*, 2017, **355**, eaad4998.
30 J. Kibsgaard, C. Tsai, K. Chan, J. D. Benck, J. K. Nørskov, F. Abild-Pedersen and T. F. Jaramillo, *Energy Environ. Sci.*, 2015, **8**, 3022–3029.
31 T. R. Hellstern, J. D. Benck, J. Kibsgaard, C. Hahn and T. F. Jaramillo, *Adv. Energy Mater.*, 2015, 1501758.
32 H. Wang, T. Deutsch, A. Welch and J. A. Turner, *Int. J. Hydrogen Energy*, 2012, **37**, 14009–14014.
33 F. Chen, Q. Zhu, Y. Wang, W. Cui, X. Su and Y. Li, *ACS Appl. Mater. Interfaces*, 2016, **8**, 31025–31031.
34 C. G. Read, J. F. Callejas, C. F. Holder and R. E. Schaak, *ACS Appl. Mater. Interfaces*, 2016, **8**, 12798–12803.
35 R. Butz, G. W. Rubloff and P. S. Ho, *Journal of Vacuum Science & Technology A*, 1982, **1**, 771–775.
36 E. G. Colgan, J. P. Gambino and Q. Z. Hong, *Mater. Sci. Eng., R*, 1996, **16**, 43–96.
37 M. Qin, V. M. C. Poon and S. C. H. Ho, *J. Electrochem. Soc.*, 2001, **148**, G271–G274.
38 R. T. P. Lee, L. T. Yang, T. Y. Liow, K. M. Tan, A. E. J. Lim, K. W. Ang, D. M. Y. Lai, K. M. Hoe, G. Q. Lo, G. S. Samudra, D. Z. Chi and Y. C. Yeo, *IEEE Electron Device Lett.*, 2008, **29**, 89–92.
39 Q. He, W. M. Huang, X. Y. Gao and M. H. Hong, *Smart Mater. Struct.*, 2005, **14**, 1320–1324.
40 H. Jiang, C. S. Petersson and M. A. Nicolet, *Thin Solid Films*, 1986, **140**, 115–130.
41 G. J. van Gurp and C. Langereis, *J. Appl. Phys.*, 1975, **46**, 4301–4307.
42 N. Biunno, J. Narayan, S. K. Hofmeister, A. R. Srivatsa and R. K. Singh, *Appl. Phys. Lett.*, 1989, **54**, 1519.
43 J. Libardi, K. G. Grigorov, M. Massi, A. S. da Silva Sobrinho, R. S. Pessoa and B. Sismanoglu, *Vacuum*, 2016, **128**, 178–185.
44 B. Avasarala and P. Haldar, *Electrochimica Acta*, 2010, **55**, 9024–9034.
45 Z. Pan, Y. Xiao, Z. Fu, G. Zhan, S. Wu, C. Xiao, G. Hu and Z. Wei, *J. Mat. Chem. A*, 2014, **2**, 13966–13975.
46 S. K. Choi, W.-S. Chae, B. Song, C.-H. Cho, J. Choi, D. S. Han, W. Choi and H. Park, *J. Mater. Chem. A*, 2016, **4**, 14008–14016.

47 A. Catellani and A. Calzolari, *Phys. Rev. B*, 2017, **95**, 115145.
48 M. W. Chase Jr, J. L. Curnutt, J. R. Downey Jr, R. A. McDonald, A. N. Syverud and E. A. Valenzuela, *J. Phys. Chem. Ref. Data*, 1982, **11**, 695–940.
49 C. E. Nebel, *Nat. Mater.*, 2013, **12**, 780–781.
50 C.-T. Li, S.-R. Li, L.-Y. Chang, C.-P. Lee, P.-Y. Chen, S.-S. Sun, J.-J. Lin, R. Vittal and K.-C. Ho, *J. Mater. Chem.*, 2015, **3**, 4695–4705.
51 FILMETRICS. Reflectance Calculator Https://www.Filmetrics.com/Reflectance-Calculator, 2018.
52 D. V. Esposito, I. Levin, T. P. Moffat and A. A. Talin, *Nat. Mater.*, 2013, **12**, 562–568.
53 C. Ros, T. Andreu, M. D. Hernández-Alonso, G. Penelas-Pérez, J. Arbiol and J. R. Morante, *ACS Appl. Mater. Interfaces*, 2017, **9**, 17932–17941.
54 M. T. Postek and A. E. Vladar, *Scanning*, 2008, **30**, 457–462.
55 P. Jiang, Q. Liu and X. Sun, *Nanoscale*, 2014, **6**, 13440–13445.
56 T. Shinagawa, A. T. Garcia-Esparza and K. Takanabe, *Sci. Rep.*, 2015, **5**, 163.
57 D. D. Smith, P. J. Cousins, A. Masad, A. Waldhauer, S. Westerberg, M. Johnson, X. Tu, T. Dennis, G. Harley, G. Solomon, S. Rim, M. Shepherd, S. Harrington, M. Defensor, A. Leygo, P. Tomada, J. Wu, T. Pass, L. Ann, L. Smith, N. Bergstrom, C. Nicdao, P. Tipones and D. Vicente, IEEE, 2012, pp. 1594–1597.
58 M. Cabán-Acevedo, M. L. Stone, J. R. Schmidt, J. G. Thomas, Q. Ding, H.-C. Chang, M.-L. Tsai, J.-H. He and S. Jin, *Nat. Mater.*, 2015, **14**, 1245–1251.
59 M. G. Walter, E. L. Warren, J. R. McKone, S. W. Boettcher, Q. Mi, E. A. Santori and N. S. Lewis, *Chem. Rev.*, 2010, **110**, 6446–6473.
60 B. Mei, A. A. Permyakova, R. Frydendal, D. Bae, T. Pedersen, P. Malacrida, O. Hansen, I. E. L. Stephens, P. C. K. Vesborg, B. Seger and I. Chorkendorff, *J. Phys. Chem. Lett.*, 2014, 3456–3461.
61 A. V. Naumkin, A. Kraut-Vass, S. W. Gaarenstroom and C. J. Powell, 2000.
62 M. F. Hochella Jr. and A. H. Carim, *Surface Science*, 1988, **197**, L260–L268.
63 H. Döscher, J. L. Young, J. F. Geisz, J. A. Turner and T. G. Deutsch, *Energy Environ. Sci.*, 2016, **9**, 74–80.
64 A. B. Laursen, R. B. Wexler, M. J. Whitaker, E. J. Izett, K. U. D. Calvinho, S. Hwang, R. Rucker, H. Wang, J. Li, E. Garfunkel, M. Greenblatt, A. M. Rappe and G. C. Dismukes, *ACS Catal.*, 2018, **8**, 4408–4419.
65 T. Saga, *NPG Asia Mater.*, 2010, **2**, 96–102.
66 Z. Chen, H. N. Dinh and E. Miller, *Springer Science & Business media: New York*, 2013.

Table of Contents Figure

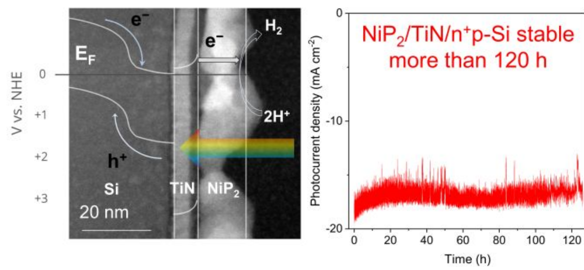

Thin-films of cubic-NiP_2 and TiN layers are applied on Si for efficient and stable photocathodes.